



## *Experimental Division*

ALBA Project Document No:

**EXD-BL13OP-GD-0001**

EDMS Document No.

Created: 20/10/2005

Pages: 32

Modified: 22/05/2006

Rev. No.: 1

### *Conceptual design of the Macromolecular Crystallography Beamline (XALOC)*

#### *Abstract*

This document is the final conceptual design of the optics of the Macromolecular Crystallography beamline (XALOC) at ALBA Synchrotron Facility.

*Prepared by:*

**Jordi Juanhuix  
Salvador Ferrer**

*Checked by:*

*Approved by:*

*Distribution List*

# *Contents*

<b>1 OVERVIEW .....</b>	<b>3</b>
1.1 Introduction	3
1.2 Beamline overview	3
<b>2 SOURCE .....</b>	<b>4</b>
2.1 Source parameters	4
2.2 Source flux	5
2.3 Source sizes and divergences	5
2.4 Source power	6
<b>3 GENERAL OPTICAL DESCRIPTION .....</b>	<b>7</b>
3.1 Optical lay-out	8
3.1.1 Adjusting the beam size at sample position	9
3.2 Spot sizes and divergences	9
3.3 Flux at sample	11
3.4 Energy resolution	12
3.5 Power load on beamline components	13
3.5.1 The power on the vacuum window	14
3.6 Ancillary branch	15
3.6.1 Optical lay-out	15
3.6.2 Beam characteristics	15
<b>4 THE DIAMOND FILTER / LAUE MONOCHROMATOR .....</b>	<b>16</b>
4.1 Functionality	16
4.2 Transmission	16
4.3 Power load	16
4.4 Footprint at the diamond filter	17
<b>5 THE MONOCHROMATOR.....</b>	<b>18</b>
5.1 Functionality and scanning mechanism	18
5.1.1 The Bragg angle	18
5.1.2 The channel cut and the fixed exit designs	19
5.2 Positional analysis	20
5.2.1 Height of the exit beam	20
5.2.2 Beam travel along the second crystal	21
5.2.3 Additional adjustments in a channel-cut design	21
5.2.4 Misalignments in a channel-cut design	22
5.3 Power load	23
<b>6 THE FOCUSING OPTICS: KB MIRROR MOUNTING .....</b>	<b>25</b>
6.1 Functionality	25
6.2 Beam footprint	25
6.3 Effect of the slope errors	26
6.3.1 Short-period slope errors	26
6.3.2 Long-period slope errors	26
6.3.3 Reducing the effect of long-period slope errors	29
<b>7 SUMMARY .....</b>	<b>30</b>
<b>8 BIBLIOGRAPHY .....</b>	<b>32</b>

# 1 Overview

## 1.1 Introduction

CELLS is a consortium created to construct and exploit the ALBA synchrotron facility to generate X rays for basic and applied research. The facility, which will be located near Barcelona, will include a 3-GeV, low-emittance storage ring able to run in top-up mode, which will feed an intense photon beam to a number of beamlines. These are placed tangentially to the storage ring and hold the experimental facilities. One of the beamlines to be implemented in the first phase of the project will be devoted to macromolecular crystallography (MX) experiments using X-rays generated by an in-vacuum undulator.

This document is organized as follows. Chapter 2 describes the photon source of the beamline, chapter 3 gives a general description of the beamline optics. Chapters 4-6 are devoted to the detailed description of active optical elements, the diamond filter, the monochromator and the KB mirrors, respectively. The contents of this document are summarized in chapter 7.

## 1.2 Beamline overview

The scientific case of this beamline has been extensively discussed in the proposal made by Spanish community, in the Scientific Advisory Committee (II meeting of SAC), and in meetings with qualified advisors (AXD-MXBO-DG-0603). Some general important conclusions are:

- The beamline has to be able to cope with the structural problems related to large complexes, which usually crystallize in large unit cells and relatively large crystals ( $\sim 200 \mu\text{m}$ ). At the same time the more conventional work involving small crystals has to be ensured to satisfy the needs of the scientific users community. To this aim, a flexible optical design involving variable focusing optics has been incorporated into the beamline optical design.
- The MX beamline has to be able to exploit the anomalous diffraction to solve the phase problem in macromolecular crystallography measurements. It is therefore important that the energy delivered by the beamline can be easily tuned in the range between 5 and 15 keV.
- In the following years from now many MX beamlines will be available for users in Europe. Therefore, this beamline has to be open to the new developments that are coming in this field. This includes new beamline optics, control, experimental techniques and robotization.

The beamline proposal and further considerations lead to define the general requirements to be fulfilled by the beamline (table 1). The resulting beamline design is presented in this document. The MX beamline at ALBA, XALOC, will be fed by a pure permanent magnet (PPM) in-vacuum undulator, which will provide high brilliance and flux density in the energy range 5-15 keV. The front-end includes the radiation safety equipment and transmits the beam in an angular aperture of  $0.4 \times 0.2 \text{ mrad}^2$  (H $\times$ V) which can be further reduced by the cooled white beam slits. Outside the shielding wall, the X rays will be filtered by a CVD diamond vacuum window and a diamond filter, and monochromatized by a Si(111) monochromator. Finally, the monochromatic beam will be focused onto the sample or the detector by a pair of mirrors placed in a KB configuration. The experimental station will include all the equipment needed to perform both wavelength independent experiments (MR, MIR, SIR) and wavelength-selective ones (MAD, SAD, SIRAS).

Source	In-vacuum PPM undulator
Optics	Si(111) monochromator KB focusing system
Photon Energy Range	5-15 keV
Photon flux at sample	$10^{12}$ ph/s in $0.1 \times 0.1$ mm <sup>2</sup>
Energy resolution	$\Delta E/E \sim 2 \cdot 10^{-4}$
Energy stability	$\pm 0.1$ eV for 3 hours
Beam size at sample (FWHM)	Adjustable 50-200 $\mu$ m (H) Adjustable 20-100 $\mu$ m (V)
Beam divergence at sample (FWHM)	$<0.5$ mrad, $<0.3$ mrad for large unit cells

**Table 1.** General requirements to the MX beamline.

Additionally, an interesting option is to use, in the diamond filter, a single diamond crystal of good crystalline quality, so that it would operate not only as a filter but also as a Laue single-crystal monochromator, delivering a diffracted beam that could feed an ancillary branch. As this Laue monochromator is dispersive, only one fixed wavelength would be collected by this branch, whereas the rest of the radiation would be absorbed or transmitted to the main one. This concept has already been proved effective in beamlines ID10 and ID14 at the ESRF.

To reduce the costs to the minimum, no optics is foreseen in this branch for the moment. In the beginning of operation, it would be dedicated to test the instrumentation to be put in the main beamline (and eventually other beamlines). In a longer term scenario, this ancillary branch could be equipped with basic instrumentation to perform MX data collection. Regarding the space availability in the Experimental Hall, it may fill the space left by the upstream bending magnet beamline, which has been cancelled due to collision of the bending magnet beam with the in-vacuum undulator chamber.

## 2 Source

### 2.1 Source parameters

The photon source of the XALOC beamline is the in-vacuum undulator IVU21, placed in the 5<sup>th</sup> medium straight section of the ALBA storage ring [1]. Main parameters of the undulator are shown in table 2. The undulator has been designed in a way that the energy of the 7<sup>th</sup> harmonic is close to 12.658 keV at a minimum gap. In this way the undulator is optimised for MX experiments, since the flux is maximum at the most commonly used energy, which corresponds to the Se K-edge.

The storage ring is planned to be operated at a nominal current of 250 mA, although the storage ring has been designed to be able to operate at a current of 400 mA. Flux calculations assume the nominal value, whereas power calculations assume the nominal or the maximum values depending on specified conditions.

Type of ID		FeCo, Pure Permanent Magnet, in-vacuum undulator	
Period	$\lambda_u$	mm	21,3
Number of periods	$N$	#	92
$K$ (at minimum gap = 5,5mm)		#	1.5949
Magnetic length	$L$	mm	1986

**Table 2.** Characteristics of the IVU21 undulator. Sizes and divergences are given in full width at half maximum (FWHM).

## 2.2 Source flux

The tuning curve for the flux delivered by the IVU21 in the energy range of interest (5-15 keV) and for gaps above 5.5 mm is shown in figure 1. Note that the energy range 5-5.3 keV can be reached by this undulator only when the gap is 5.2-5.5 mm, that is, below the nominal value of 5.5 mm. Therefore, this energy range can only be accessible when the operation of the machine and the beamline will allow closing the gap further down to the nominal value.

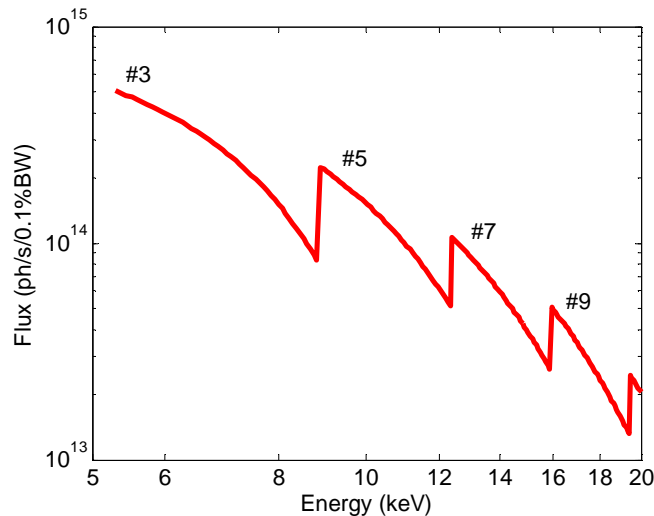


**Figure 1.** Output flux of the IVU21 in the range of interest. The energy of the 7<sup>th</sup> harmonic at minimum gap is close to the Se K-edge (12.658 keV). Current in ALBA storage ring is assumed to be 250mA.

## 2.3 Source sizes and divergences

Photon beam sizes and divergences of the undulator source are mainly limited by the sizes and divergences of the electron beam circulating in the storage ring. The vertical divergence is also also contributed by the effect of the electron energy spread [2], which has about the same value than the electron beam divergence. Sizes and divergences are constant in the energy range of interest (table 3), except for the vertical divergence, which nevertheless varies only by about 20% (Fig. 2)

Photon source size (H×V)	$\Sigma_{x,y}$	$\mu\text{m}$	$309 \times 18$
Photon source divergence (H×V)	$\Sigma'_{x,y}$	$\mu\text{rad}$	$112 \times 28\text{--}22$

**Table 3.** Beam sizes and divergences delivered by the undulator source. Values are given in full width at half maximum (FWHM). Note that these dimensions refer to the flux profile at a given energy in the range 5-15 keV. Power profiles are much wider (Fig. 4).

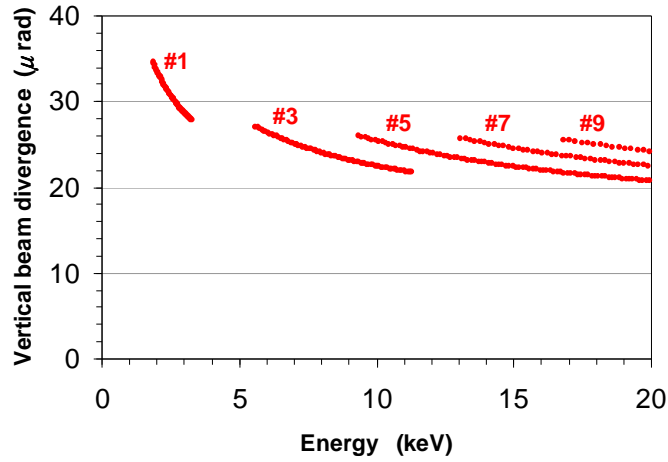


**Figure 2.** Vertical photon source divergence in the energy range of interest. Values are given in full width at half maximum (FWHM). The other source divergence and sizes are constant in this range (Table 3).

## 2.4 Source power

The integrated power delivered by the undulator depends on the tuned energy of the undulator (Fig. 3) since this is selected by changing the gap and thus the K-value. At minimum gap (5.5 mm), the delivered power is maximum and is as high as 2.87 kW when the current in the storage ring is 400mA. The power distribution is approximately gaussian, with a maximum power density of 24.8 kW/mrad<sup>2</sup> (Fig. 4).

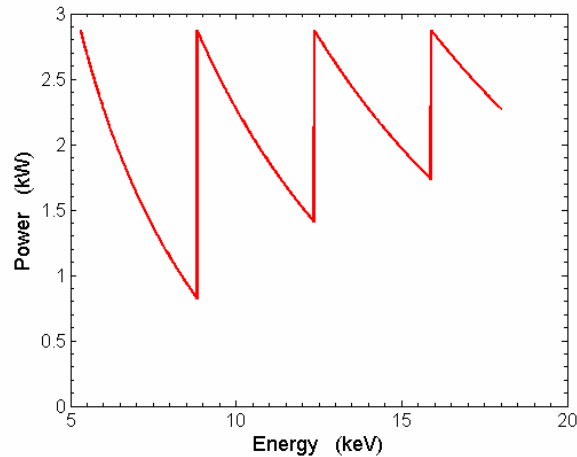


**Figure 3.** Power delivered by the undulator in function of the tuned energy. Current in the storage ring is assumed to be 400 mA.

Nevertheless, part of radiation is absorbed by the front-end. The angular aperture of the front-end is  $\pm 0.2$  mrad and  $\pm 0.1$  mrad in the horizontal and vertical directions, respectively. This limited acceptance reduces to ca. 1.5 kW the maximum power incoming to the beamline optics, the front end absorbing 1.4 kW, assuming a current of 400 mA in the storage ring. White beam slits installed inside of the shielding wall will allow further reducing the power incoming to the beamline.

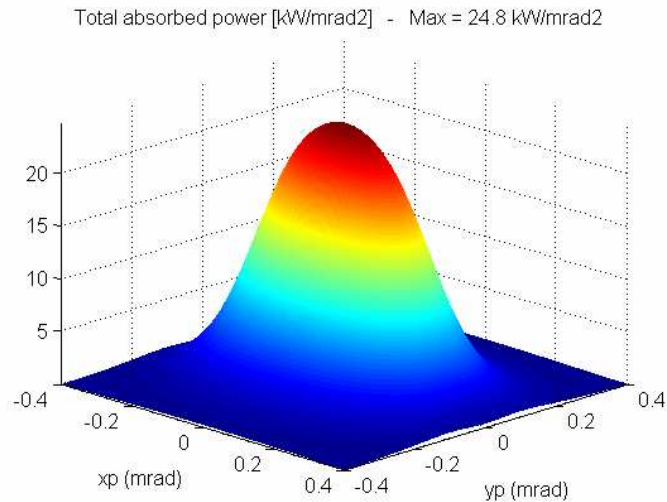


**Figure 4.** Angular power density (in kW/mrad<sup>2</sup>) delivered by the IVU21 undulator. Current in storage ring is assumed to be 400 mA.

### 3 General optical description

The XALOC beamline will be installed at the straight section num. 10 of the ALBA storage ring. The optics will consist of a diamond filter to protect the downstream optics from excessive power, a non-dispersive Si(111) monochromator and a KB focusing optics (Fig. 5). As required, this optics can deliver a tuneable X-ray beam with adjustable beam size at sample position.

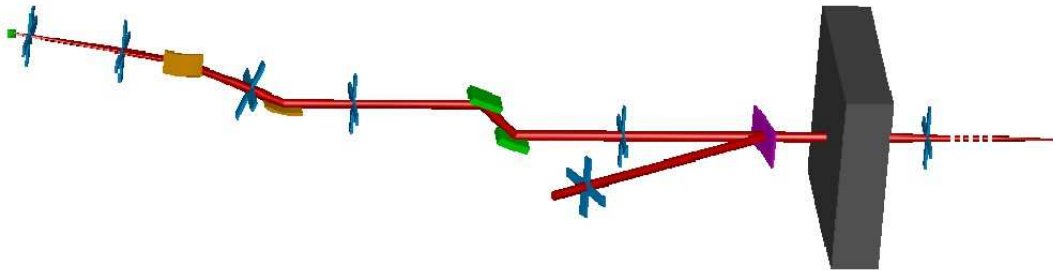


**Figure 5.** Lay-out of the MX beamline, showing the main beamline and the ancillary branch.

It has been considered interesting as a simple, low-cost and technically sound option, to use a diamond single crystal of good crystalline quality as a filter in order to be operated as well as a Laue single-crystal monochromator which would generate a diffracted beam. This beam might be used as an ancillary branch of the beamline for testing instruments. The ancillary branch may fill the space left by the upstream bending magnet beamline, which has been cancelled due to collision of the bending magnet beam with the in-vacuum undulator chamber. To reduce the costs to the minimum, no optics is envisaged in the ancillary branch for the moment although, if financially possible, it would be useful to install a pair of motorized slits and a precision table to mount instruments.

The general optical descriptions of the beamline and the putative ancillary branch are given in this chapter. More detailed description of the active optical elements of the beamline (i.e. diamond filter, monochromator and KB mirrors) is given in the following chapters.

### 3.1 Optical lay-out

The optics of the main branch consists in a vacuum window, a diamond filter, a channel-cut Si(111) monochromator and a pair of mirrors in a Kirkpatrick-Baez (KB) configuration [5] (Fig. 6). The monochromator selects a given energy, with a narrow band pass, from all the spectrum delivered by the undulator, and absorbs most of the incoming power. Symmetric Si(111) reflection is chosen since the energy resolution it provides matches properly the needs of MAD experiments in the energy range of interest. The KB mirrors focus onto the sample or the detector, the first one (coming from the source) in the vertical direction, and the other one in the horizontal one. The vertical and horizontal focusing mirrors demagnificate the source by a factor of 3.84 and 6.58, respectively. The demagnification factors compromise the beam size and divergence at sample position.

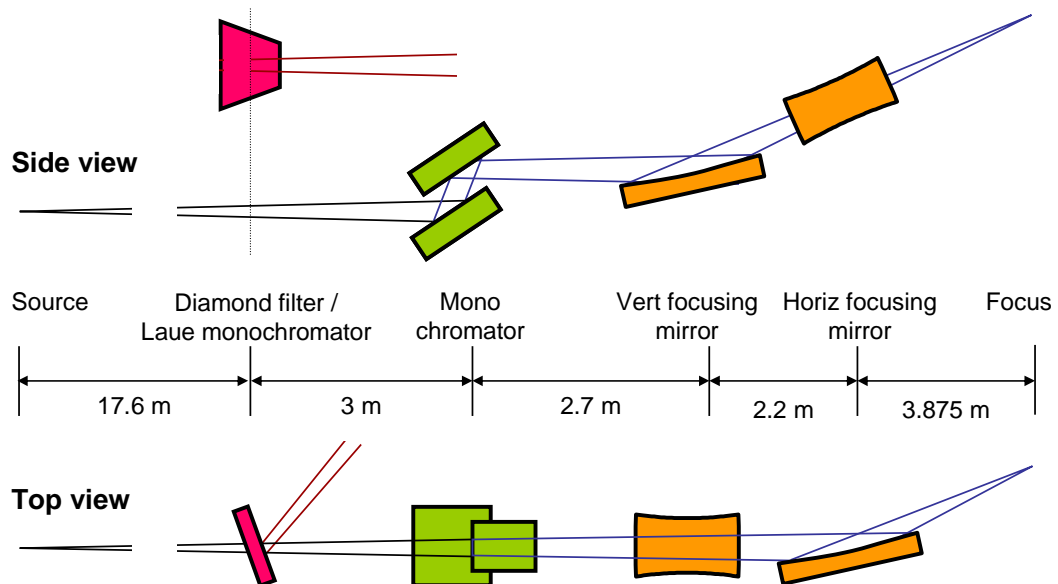


**Figure 6.** Schematical lay-out of the XALOC beamline, including the main beamline and the ancillary branch.

The list of optical components of the XALOC beamline is shown in table 4, together with their brief description and distance from source to the beginning of the element. In addition to these optical elements, a complete set of beam defining slits and a complete set of diagnostics devices after each major optical element. The diagnostics is especially important in order to achieve good beam stability and high reliability of the beamline, which is a major concern in the design.

Optical element	Distance from source	Description
CVD diamond Vacuum window	17 m	Isolates the vacuum of the beamline Absorbs power
Diamond filter (Laue monochromator)	17.6 m	Absorbs power (Provides beam to ancillary branch)
Si (111) monochromator	20.6 m	Selects the energy
Vertical Focusing Mirror (VFM)	23.3 m	Focuses vertically the beam
Horizontal Focusing Mirror (HFM)	25.5 m	Focuses horizontally the beam

**Table 4.** Beamline optical components.

### 3.1.1 *Adjusting the beam size at sample position*

An important and tight requirement of the beamline is to have an adjustable beam size at sample position to match it to the crystal size. Moreover, whenever possible, the beam size at the detector should not be much larger than the point spread function (PSF) of the detector to avoid losing resolution.

The beam size at sample will be adjusted in the XALOC beamline by defocusing, that is, to focus the beam out of the sample position, preferable onto the detector or close to it. The beam is then broader at the sample position. However, when working out of focus, the beam profile at sample is very sensitive to the slope errors of the optical surfaces, especially in the low-frequency range. This is discussed in chapter 6.

Suitable beam homogeneity is especially difficult to achieve in the vertical direction due to the small beam size and divergence in this direction. In the case that the vertical beam unhomogeneities affected the data collection, it would be very convenient to be able to remove the vertical focusing mirror from the beam path. By removing it the beam would preserve the original gaussian profile given by the undulator source at the sample position. In this case, the beam size should be adjusted using slits close to the sample.

## 3.2 **Spot sizes and divergences**

We discuss here the spot sizes and divergences at sample and focal positions, modelled using SHADOW through a Matlab interface [3]. Note that no slope errors are assumed here, as they are discussed in chapter 6.

The focal spot size of the beamline without slope errors is  $50 \times 5 \mu\text{m}^2$  (H×V) FWHM (Fig. 7). The detector is assumed to be in the focal position, so the sample will be placed out of focus. The spot size at sample will then change depending on the distance between the sample and the detector. For example, to have data at  $2\text{\AA}$  resolution using X rays at 12.658 keV and a detector

having a diameter of 315mm, the distance must be 379 mm. In this position, the spot size at sample is  $195 \times 33 \mu\text{m}^2$  (H $\times$ V) FWHM. Changing the distance and/or defocusing in one or both dimensions will change the spot dimension. These dimensions are practically independent of the photon energy.

It is worth remarking that the beam size at detector position can be as large as  $100 \mu\text{m}$  without degrading significantly the performance of the beamline. This is so because this is roughly the value of the point spread function (PSF) of the best detectors currently available, based in the CCD technologies. The apparent beam dimension at the detector will be, at least, the value of the PSF, so experiments will not take advantage of a better focusing at the detector.

The beam divergence at sample is about  $0.57 \times 0.09 \text{ mrad}^2$  (H $\times$ V) FWHM at 12.658 keV (Fig. 8). The divergence can be reduced by cutting the beam using the slits close to the focusing mirrors, at the expense of reducing proportionally the flux onto the sample. The horizontal divergence is limited by the acceptance of the horizontal focusing mirror.

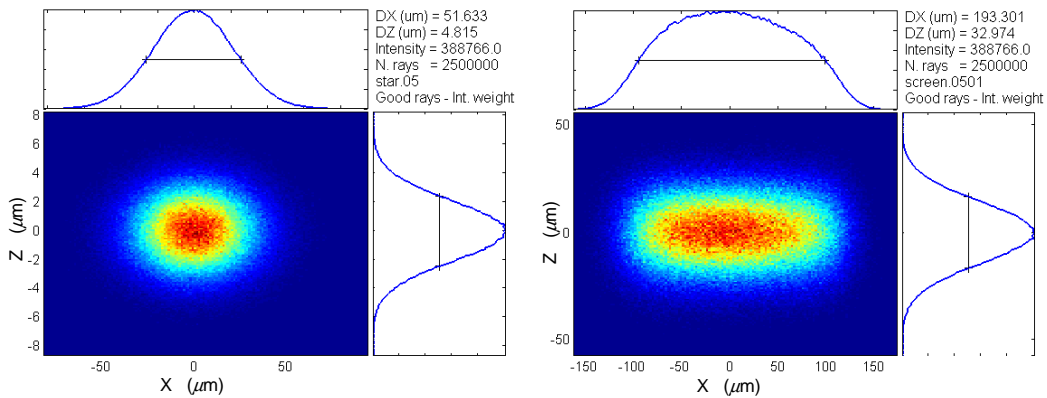


**Figure 7.** Raytracing simulation of the spot sizes at detector position (focused beam) (*left*) and at sample position (379mm before focus) (*right*). Mirror acceptance is included.

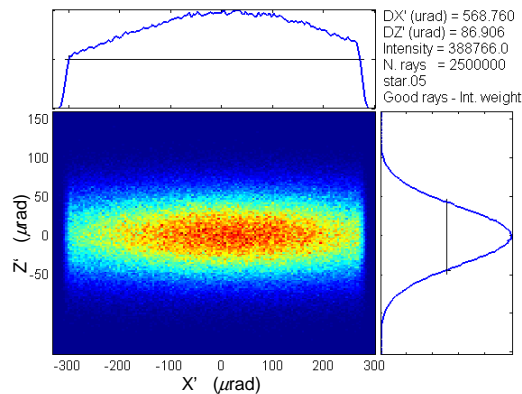


**Figure 8.** Raytracing simulation of the beam divergence/convergence at sample. Mirror acceptance is included.

As it has been said before, the vertical focusing mirror should be removable in case its slope errors introduced unacceptable unhomogeneities to beam at sample or detector positions. In this case, as the beam remains unfocused in the vertical dimension, the beam size in this direction increases to about  $700\ \mu\text{m}$  (Fig. 9). In this situation, clearly the beam shall be slit down vertically to adjust the beam size to the crystal dimensions. Nevertheless, an important advantage of this configuration is that the vertical divergence of the beam is that of the source, which is only about  $25\ \mu\text{rad}$ .

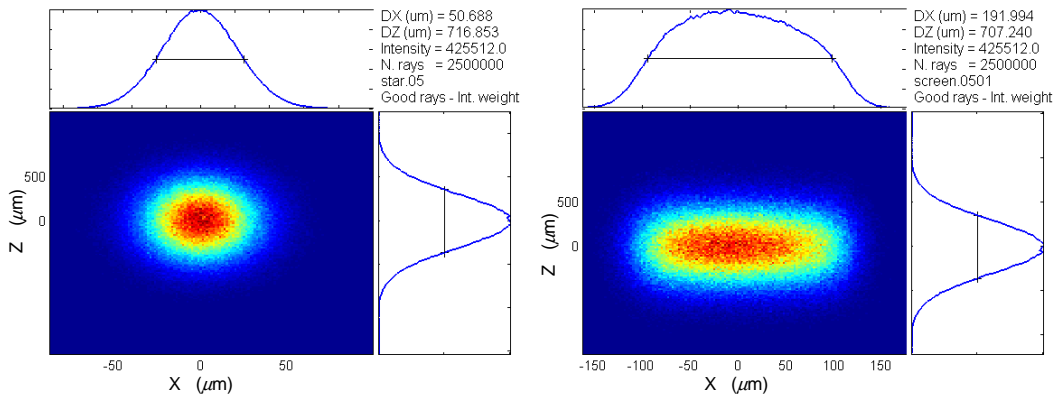


**Figure 9.** Raytracing simulation of the spot sizes when the vertical focusing mirror is removed at detector position (focused beam) (*left*) and at sample position (379mm before focus) (*right*). Horizontal focusing mirror acceptance is included.

### 3.3 Flux at sample

The flux of the beamline at sample is essentially proportional to the flux delivered by the undulator in the central cone because the source dimensions are essentially unaltered in the energy range of interest, so is the acceptance of the mirrors. In addition, other multiplicative factors are also constant, namely, the reflectivity of the mirrors and the energy band pass for each monochromator. Taking into account these considerations, as well as the transmission of the diamond crystal, the calculated flux of the main branch at sample position is above  $3 \cdot 10^{12}$  ph/s in the whole energy range, assuming a current of 250 mA in the storage ring and including a symmetric monochromator (Fig. 10). This fulfils the requirement on flux listed in table 1.

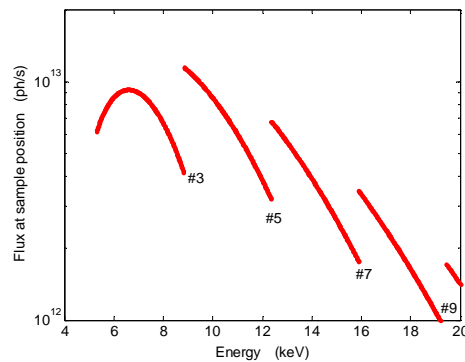


**Figure 10.** Calculated flux of the main branch at sample position assuming an current in the storage ring of 250 mA. The model includes vacuum window transmission ( $300\ \mu\text{m}$ -thick, diamond), monochromator, and reflectivity and acceptance of the mirrors.

### 3.4 Energy resolution

The energy resolution  $\Delta E/E$  provided by the beamline is contributed by two terms, namely, the natural divergence of the source in the dispersive direction  $\Sigma'_y$ , and the crystal Darwin width of the incoming beam  $\omega_{D, inc}$ . In a first approximation these two contributions can be added quadratically, so the overall resolution is

$$\frac{\Delta E}{E} = \sqrt{\omega_{D, inc}^2 + \Sigma_y'^2} \cot \theta .$$

For symmetric Si(111) and the photon beam vertical divergence being that of the natural divergence of the undulator, the calculated energy resolution is less than  $\Delta E/E = 2 \cdot 10^{-4}$  in the 5-15 keV energy range (Fig. 11), fulfilling the beamline requirement. The resolution deteriorates at higher energies due to the smaller Bragg angles, which make the energy more sensitive to the slightly different incidence angles of the divergent beam onto the crystal.

Raytracing simulations agree with the analytical expression. At 12.658 keV the simulation gives a value of the energy resolution of  $1.8 \cdot 10^{-4}$  (Fig. 12), which compares well with the one obtained with analytical expressions,  $1.77 \cdot 10^{-4}$ .

Regarding beam stability, this was set to be  $\pm 0.1$  eV (Table 1). As the energy bandpass has a FWHM of about 2 eV, this represents a variation of 10%, which is enough to perform standard MAD experiments.

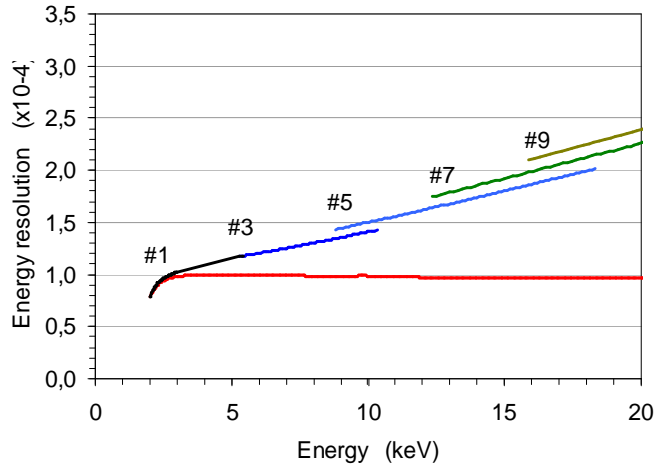


**Figure 11.** Calculated energy resolution  $\Delta E/E$  provided by the Si(111) monochromator in the XALOC beamline. The beam divergence and Darwin width (in red) contributions are added using RMS, and the result is converted to FWHM in the plot. Note that this value is the FWHM of the equivalent gaussian of the rocking curve, so its value differs from the original FWHM of the rocking curve (which is about  $1.4 \cdot 10^{-4}$  for symmetric Si(111), instead of  $1.0 \cdot 10^{-4}$  as shown in red).

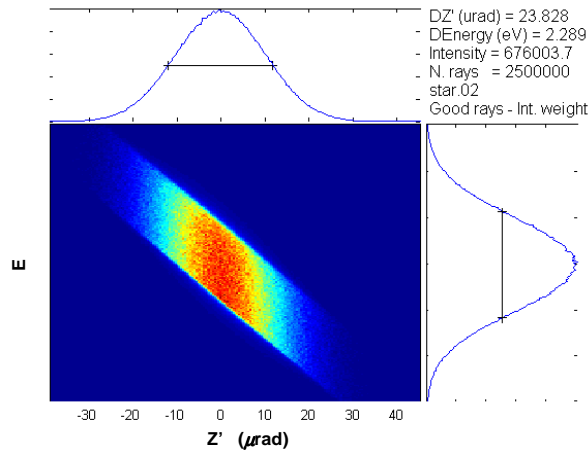


**Figure 12.** Raytraced Dumond diagram (with wavelength replaced by photon energy) of the beamline with a symmetric monochromator. X-Y axes are vertical divergence (in  $\mu\text{rad}$ ) and energy (in eV), respectively.

### 3.5 Power load on beamline components

The power from the source is filtered successively by the Front-end fixed masks, the white beam slits, the vacuum window, the diamond filter and the monochromator. The absorbed power and power density of the latter 3 elements, which are the most sensitive elements, are listed table 5.

	Working conditions 250 mA Slits matched to mirror acceptance 0.112×0.054 mrad <sup>2</sup>	Working conditions 250 mA Slits matched to mirror acceptance 0.112×0.054 mrad <sup>2</sup>	Worst case conditions 400 mA Full front-end acceptance 0.4×0.2 mrad <sup>2</sup>
Incoming power	90.5 W	90.5 W	1482 W
Power absorbed at the vacuum window	46.6 W (44.3 W/mm <sup>2</sup> )	46.6 W (44.3 W/mm <sup>2</sup> )	885 W (44.3 W/mm <sup>2</sup> )
Power absorbed at the diamond filter	9 W (4.6 W/mm <sup>2</sup> )	(removed)	143 W (7.4 W/mm <sup>2</sup> )
Power absorbed at the monochromator	34.9 W (5.6 W/mm <sup>2</sup> )	43.9 W (7 W/mm <sup>2</sup> )	454 W (9 W/mm <sup>2</sup> )

**Table 5.** Power budget of XALOC beamline. The mirror acceptance in working conditions is such that covers 1 FWHM and 2 FWHM of the beam in the horizontal and vertical directions, respectively. The power on the monochromator at worst-case conditions with the diamond filter being removed is 597 W, with a power density of 11.2 W/mm<sup>2</sup> and 3.7 W/mm<sup>2</sup> at 5 and 15 keV, respectively.

The power on the optical elements strongly depends in the acceptance of the white beam slits. In the case they are fully open, all the beam accepted by the front end, which amounts to ca. 1.5 kW at a current of 400 mA in the storage ring, arrives at the beamline. These are the *worst-case conditions*. More realistic conditions are attained when the white beam slits are matched to the acceptance of the mirrors, and a current of 250 mA is assumed to circulate in the storage ring. In these *working conditions*, the power incoming to the beamline is about 90 W, from which half of the power is absorbed by the vacuum window.

A more detailed analysis and the power distributions on the diamond filter and the channel-cut monochromator is given in chapter 4 and 5, respectively.

### 3.5.1 The power on the vacuum window

The power distribution on the CVD diamond vacuum window in worst-case conditions is shown in figure 13. Recent measurements done at ESRF (J.C. Biasci, private communication) show that 300  $\mu\text{m}$ -thick CVD diamond of a diameter of 6mm can withstand total absorbed powers of  $\sim 500$  W and absorbed power densities of  $\sim 70$  W/mm<sup>2</sup> using water cooling. These values are much higher than those calculated for this beamline at working conditions. However, they can still be a concern when working under the worst-case conditions, since the power absorbed by the vacuum window exceeds those found safe through these experiments. Nevertheless, the power on the vacuum window can be reduced by closing the white beam slits. For instance, by closing to the half the slits ( $0.2 \times 0.1$  mrad<sup>2</sup>), the power absorbed is reduced to less than 250 W, without any reduction on flux at sample.

The “traditional” scheme of attenuation of the white beam, that is, a combination of a pyrographite filter and a Be window could also withstand the power and power densities of the undulator when slits are closed down. In this traditional approach, two pyrographite filters of a thickness of 250  $\mu\text{m}$  each and a diameter of 2 mm can absorb a maximum power of  $\sim 450$  W with a maximum power density of 45 W/mm<sup>2</sup>. Regarding the Be window, it can absorb about with a maximum absorbed power density of 3 W/mm<sup>2</sup>. Nevertheless, this approach is disregarded due to the large amount of diffuse scattering from the pyrographite and to the somewhat higher performance of CVD diamond vacuum windows.

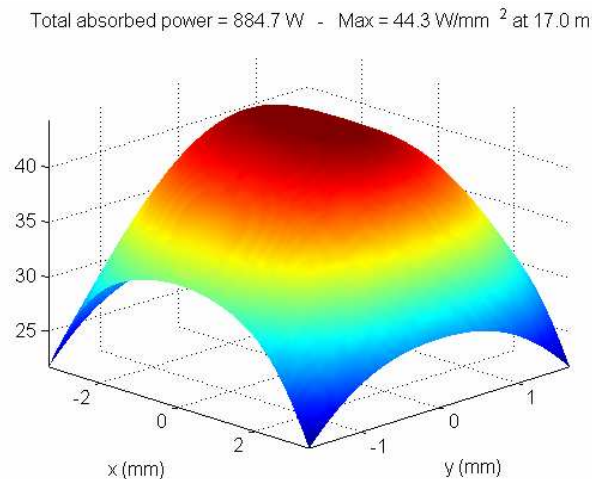


**Figure 13.** Absorbed power of a 300 $\mu\text{m}$ -thick CVD diamond vacuum window, assuming that the white beam slits accept the maximum acceptance of the Front-End ( $0.4 \times 0.2$  mrad<sup>2</sup>). The current in the storage ring is 400 mA

### 3.6 Ancillary branch

#### 3.6.1 Optical lay-out

In the case of being built, the ancillary branch would take advantage of the diamond filter already in place for the main beamline, and use it as a Laue single-crystal monochromator. This thin diamond crystal would split the beam used in this branch from the rest of the beam, which would be absorbed or transmitted to the main beamline. This Laue monochromator is the only optical element foreseen in order to simplify operation and reduce costs. The branch will be set up at a fixed energy (9.041 keV, 1.371 Å), as the Laue crystal acts as a dispersive monochromator.

The strong Si(111) reflection, suitable due to its large structure factor and the extinction of the (222) reflection, diffracts the chosen wavelength at  $2\theta = 38.90^\circ$ . Using a diamond crystal cleaved in the [100] direction, the asymmetric cut angle is  $54.736^\circ$ , and the tilt angle with respect to normal incidence is  $15.815^\circ$ .

#### 3.6.2 Beam characteristics

The ancillary branch exploits the focusing properties on polychromatic beams of the Laue monochromator [5]. Without any other optical element, the diffracted beam focuses approximately at 9 m after the Laue monochromator onto a spot of  $0.77 \times 0.55 \text{ mm}^2$  and a divergence of  $137 \times 24 \text{ } \mu\text{rad}^2$  FWHM (Fig. 14). In the vertical plane the beam is basically propagated from the source, whereas horizontally is compressed due to the asymmetric cut of the Laue crystal, at the price of a slight increase of the beam divergence (112 to  $137 \text{ } \mu\text{rad}$ ).

The energy resolution,  $\Delta E/E = 3.3 \cdot 10^{-4}$ , can be readily improved by closing the horizontal slits, as it depends on the horizontal divergence. The flux is calculated to be  $6.7 \cdot 10^{12}$  ph/s.

The energy resolution of the ancillary branch is  $\Delta E/E = 3.3 \cdot 10^{-4}$ , which is essentially contributed by the relatively large divergence in the horizontal direction. However, this can be readily improved by closing the horizontal slits, as selected energy depends on the horizontal divergence. The flux of the ancillary branch, mainly limited by the narrow Darwin width of the Diamond(111) reflection, is calculated to be  $6.7 \cdot 10^{12}$  ph/s.

Note that this beam would be well suited for applications requiring a very small divergence and moderate beam sizes, as it could be the case for large complexes crystallizing in large crystals.

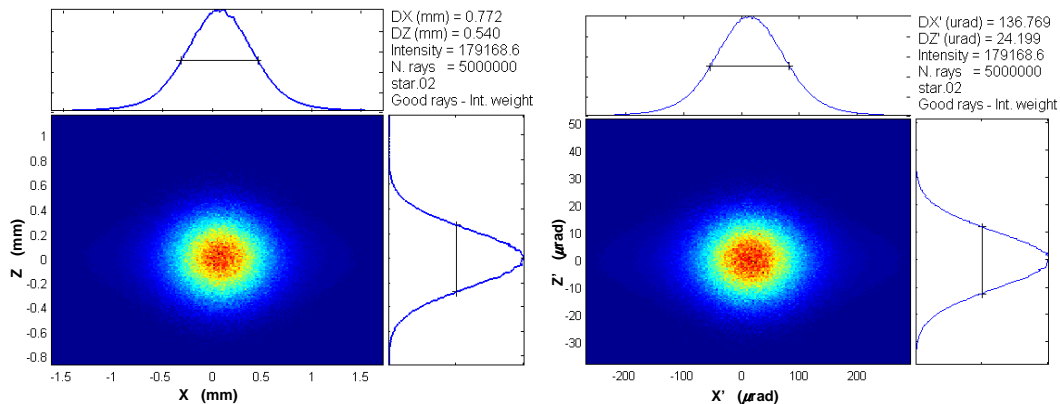


**Figure 14.** Raytracing simulation of the beam sizes (*left*) and divergences (*right*) of the side branch at 5m after the diamond filter, assumed to be a  $300 \text{ } \mu\text{m}$ -thick crystal working in Laue configuration.

## 4 The diamond filter / Laue monochromator

### 4.1 Functionality

The primary function of the diamond filter is to absorb the low-energy part of the power, which is not used by MX experiments, and avoid the thermal effects of this to the optics downstream. This function can be accomplished by using a standard CVD diamond.

Nevertheless, if the diamond is of good quality, the filter can be used as well as a Laue monochromator, which could diffract a monochromatic beam sideways onto an ancillary branch, whereas the rest of the radiation not absorbed would be transmitted downstream to the beamline. This option does not change the optical performance of the filter vis-à-vis the main beamline. See section 3.6 for details of the filter working as a Laue monochromator.

### 4.2 Transmission

The diamond crystal has to transmit a significant amount of the radiation in the whole energy range of interest (5-15 keV), while absorbing the rest of the radiation power. The effective thickness of the filter, that is, the length of the beam path inside the filter, is the key parameter to play with. An additional constraint is that the filter should be thick enough to be mechanically and thermally stable.

A good compromise between these factors appears to be a thickness of 300  $\mu\text{m}$ , which with a tilt angle of the filter of  $15.815^\circ$  corresponds to an effective thickness of 311.8  $\mu\text{m}$ . At 7 keV the transmission of the diamond filter with the diamond vacuum window is more than 20% (Fig. 15). Below 7 keV, the diamond filter should be removed to reduce the absorption. At 5 keV, with only the vacuum window in place, the transmission is about 12%.

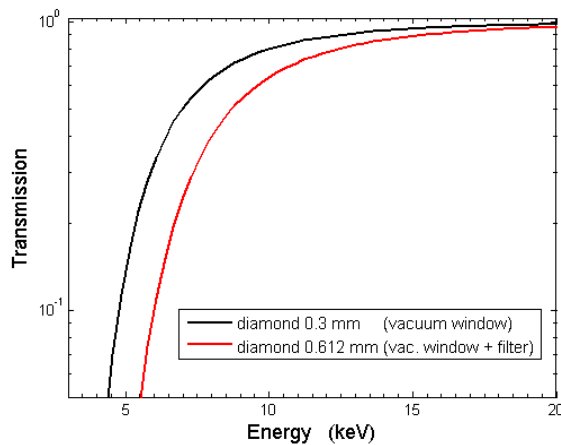


**Figure 15.** Transmission of the vacuum window (black line) and the vacuum window with the diamond filter.

### 4.3 Power load

Table 5 summarizes the power absorbed diamond filter under the *worst-case* (white beam slits fully open, the storage ring operating at 400mA) and *working conditions* (slits closed to mirror acceptance, which is  $112 \times 54 \mu\text{rad}^2$ , and a current of 250 mA in the storage ring).

Assuming a thickness of  $300\ \mu\text{m}$  and a tilt angle of  $15.815^\circ$ , the power absorbed by the diamond filter under the worst case conditions is  $143\ \text{W}$ , with a maximum power density of  $7.4\ \text{W}/\text{mm}^2$  (Fig. 16). The power footprint is relatively large, about  $9\times 4\ \text{mm}^2$ . As explained in section 3.5.1 regarding the vacuum window, these values can be well handled using designs already tested. Therefore, the diamond filter works in safe conditions even under the worst-case conditions.

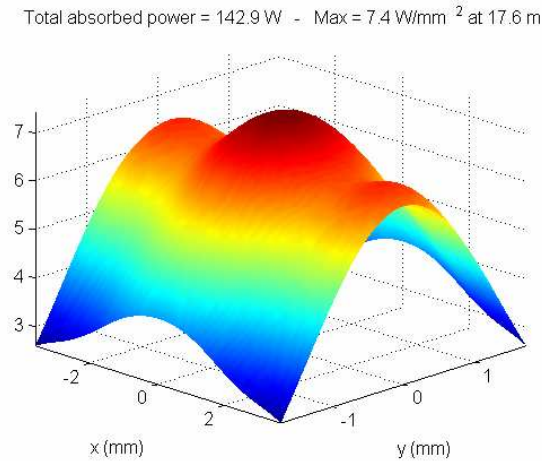


**Figure 16.** Absorbed power of a  $300\ \mu\text{m}$ -thick diamond filter tilted with respect to the beam by  $15.815^\circ$ , assuming that the white beam slits accepts the maximum acceptance of the Front-End ( $0.4\times 0.2\ \text{mrad}^2$ ). The effective thickness of the filter is  $311.8\ \mu\text{m}$ . The beam has already been filtered by a  $300\ \mu\text{m}$ -thick CVD diamond vacuum window. The current in the storage ring is  $400\ \text{mA}$ .

However, the power and power density absorbed by the diamond filter must be much lower to preserve the optical required properties to work as a Laue monochromator. In particular, we require the cooling system to be able to evacuate the thermal load without introducing a RMS deformation of the crystal greater than  $10\ \mu\text{rad}$ , which corresponds to the RMS vertical beam divergence. A higher deformation would lead to a significant broadening of the beam in the vertical direction. Finite Element Analysis has to be done to evaluate the effect of the thermal bump and to choose the cooling scheme.

An example of the absorbed power and power density that a Laue monochromator can absorb is given by the beamline I911-1 at Maxlab (Thomas Ursby, private communication). In this beamline, which has a wiggler as a photon source, a  $300\ \mu\text{m}$ -thick, unbent Laue monochromator is used under a heat load of  $10\text{-}15\ \text{W}$  and a power density of around  $1\ \text{W}/\text{mm}^2$ . The amount of absorbed power under working conditions in the XALOC beamline ( $9\ \text{W}$ ) is comparable to this beamline, although the power density ( $4.4\ \text{W}/\text{mm}^2$ ) is higher due to the source (in-vacuum undulator used in XALOC, wiggler used in I911-1). FEA is needed to validate the use of the diamond filter as a Laue monochromator in the XALOC beamline.

#### 4.4 Footprint at the diamond filter

The footprint of the beam at the diamond filter is ca.  $2\times 0.5\ \text{mm}^2\ \text{H}\times\text{V}$  (FWHM), with a gaussian profile in both directions (Fig. 17). Note that these are the dimensions of the beam in the energy range of interest, not the footprint of the white beam. The total footprint including all energies is much broader, as shown in power calculations.

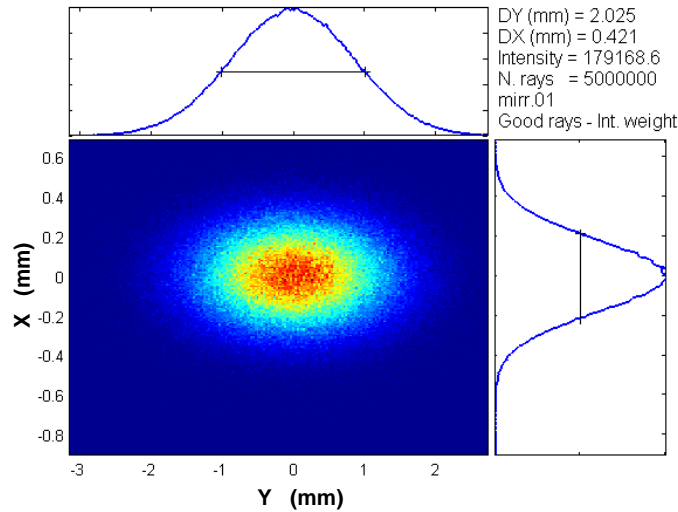


**Figure 17.** Footprint of the monochromatic beam (9.041 keV) on the diamond filter. Tilt of the filter with respect of the beam is 15.815°.

## 5 The monochromator

### 5.1 Functionality and scanning mechanism

The monochromator selects the energy at which the experiment will be carried out. Only the selected energy and its harmonics go through, while all the other energies, which amount for practically all the power of the incoming beam, are absorbed.

#### 5.1.1 The Bragg angle

The optical elements of the monochromator are 2 Si crystal surfaces placed in a non-dispersive mounting and with the optical surface oriented in the [111] direction. The energy is selected by rotating the stage in which the surfaces are held, thus changing the incident angle of the beam  $\theta$  onto the crystals (*Bragg angle*) (Fig. 18). The relation between the selected photon energy (thus the wavelength) and the Bragg angle  $\theta$  is given by the Bragg law,

$$\lambda = 2d \sin \theta,$$

where  $d$  is the interplanar spacing of the diffracting reflection of the crystal (in the case of Si(111),  $d = 3.1355\text{\AA}$ ),  $\theta$  is the angle between the beam and the crystal surface, and  $\lambda$  is the wavelength of the diffracted photons (being the energy  $E [\text{keV}] = 12.39841 \lambda [\text{\AA}]$ ). In the XALOC beamline, the experiments will be done with Bragg angle ranging from 7.574° (at 15 keV) to 23.296° (at 5 keV), although for mechanical and alignment reasons the range shall be larger.

The intrinsic angular band pass of the monochromator  $\omega_D$ , also called *Darwin width*, is related to the accuracy required to the main goniometer controlling the Bragg angle. The Darwin width is derived from the differential form of the Bragg Law,

$$\omega_D = \left( \frac{\Delta E}{E} \right)_{\text{Si}(111)} \tan \theta$$

where  $\theta$  is given by the selected energy and  $(\Delta E/E)_{\text{Si}(111)}$  is the energy bandpass intrinsic to the reflection (for Si(111),  $\Delta E/E = 1.4 \cdot 10^{-4}$ ).

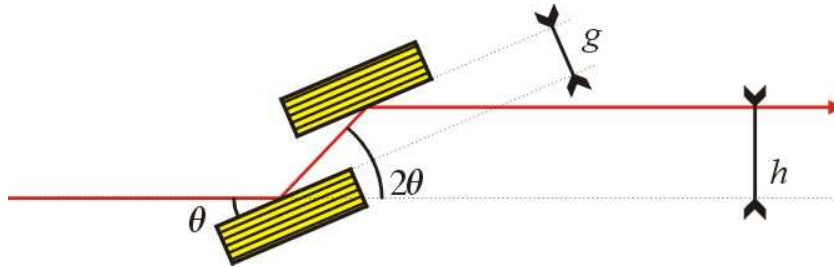


**Figure 18.** Basic lay out of the monochromator. Bragg angle  $\theta$  determines the selected energy. In the channel-cut design the two diffracting surfaces are carved in the same block, so the gap  $g$  between them is constant. In the double-crystal, fixed-exit monochromator, the crystals are adjusted independently so they provide a exit beam at a constant height  $h$ .

### 5.1.2 The channel cut and the fixed exit designs

As explained in the previous chapter, two different basic designs of the double-crystal monochromator are considered in the XALOC beamline: the channel-cut and the fixed-exit designs. In the fixed-exit design the relative position of the crystals are adjusted to provide an exit beam at fixed height  $h$  (Fig. 18). In the channel-cut design, the two optical surfaces of the monochromator are carved in the same crystal block, so the gap  $g$  between crystals is constant which eases the operation as the alignment between crystal surfaces is ensured.

Both designs have pros and cons. The fixed-exit monochromator, when is well aligned, provides a fixed beam at any energy, so the requirements on the optics downstream are less demanding. The other design, the channel-cut, is much simpler in terms of alignment, vacuum and vibrations, and cheaper, although the beam changes its height at the exit of the monochromator upon the energy. The choice between these two monochromator designs is a matter of taste and depending of the previous experience of the staff in charge at the beamline.

XALOC beamline will probably use a channel-cut monochromator. The decision is taken on the basis that good beam stability is most likely to be achieved with this design because of its simplicity, which allows a higher stiffness of the ensemble.

Finally, note that, in a channel-cut design, several channel-cut crystals can be mounted side by side on the stage, so that one of them can be selected to be placed in the beam path. This would be useful to place crystals cut along different Bragg planes, or with an asymmetry angle. However, as the vast majority of the data collections will use the symmetric Si(111) reflection, the option of placing different crystals side by side is disregarded for sake of simplicity.

## 5.2 Positional analysis

### 5.2.1 Height of the exit beam

An important drawback of the channel-cut design is that it does not provide a fixed height of the outcoming beam, but it depends on the wavelength. To follow the beam, the optics downstream and the experiment environment have to be displaced accordingly. The monochromator design has to limit as much as possible this beam height variation to simplify the beamline operation.

For symmetric crystals, the beam height  $h$  at the exit of the monochromator depends on the set-up wavelength via the Bragg angle  $\theta$ ,

$$h = 2 g \cos \theta ,$$

where  $g$  is the gap between the two diffracting crystal surfaces. In the other hand, if the crystal surfaces were asymmetrically cut with an angle  $\alpha$  (positive when turning anticlockwise from the surface to the crystal planes, i.e. in the expanding mode), the beam height would be

$$h_{asym} = 2 g_{asym} \frac{\cos \theta}{\cos \alpha + \cot \theta \sin \alpha} .$$

The effect of the channel-cut monochromator on the beam height is of the order of 1-2 millimetres (Fig. 19), and is proportional to the gap between crystals. The gap between crystals should be as small as possible to relax the strokes and tolerances (as many depend linearly on  $h$ , see below) of several movements, while avoiding the presence of shadows at large Bragg angles and ensuring the accessibility to polish the surfaces.

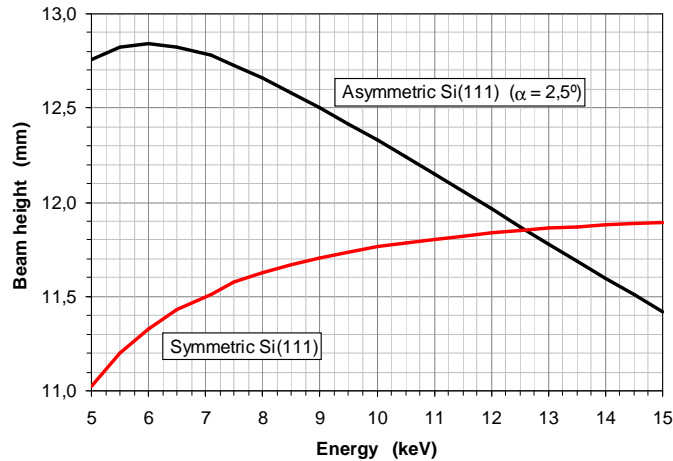


**Figure 19.** Energy dependence of the height of the beam at the exit of the symmetric (red) and asymmetric (black) channel-cut monochromators. The gaps between crystals are 6mm and 7.65mm for the symmetric and asymmetric crystals, respectively. The gap of the asymmetric crystal has been set to provide the same height as the symmetric one at 12.658 keV.

### 5.2.2 *Beam travel along the second crystal*

An important issue which depends on the gap between crystals  $g$  is the travel  $l_2$  of the beam along the surface of the second crystal as we scan in energy. This is given by

$$l_2 = g \left( \frac{1}{\tan \theta_{\max} \cos \alpha + \sin \alpha} - \frac{1}{\tan \theta_{\min} \cos \alpha + \sin \alpha} \right)$$

To put some numbers, to cover the entire energy range of the beamline (5-15 keV), and assuming the gap  $g$  to be 6 mm between two symmetric surfaces ( $\alpha = 0$ ), the beam shift along the second crystal surface is  $l_2 = 31.2$  mm.

### 5.2.3 *Additional adjustments in a channel-cut design*

Apart from the Bragg angle, the crystal needs to be oriented along other directions and rotations (see figure 20 for definitions). In the case of the channel-cut design, these are

- Pitch of the second crystal ( $\theta_2$ ): It is critical to adjust the detuning between the two crystal surfaces at any Bragg angle. It should not affect the planarity of the crystal surface. The resolution of the pitch adjustment of the second crystal has to be much smaller than the Darwin width to allow an accurate tuning of the monochromator. It is the only additional adjustment to do in the channel-cut monochromator during normal operation. A strain gauge can be used to encode the position.
- Vertical translation of the crystal ( $Z$ ): This adjustment allows the alignment of the crystal height with respect to the axis of the Bragg angle. This is needed to predict the beam height at the monochromator exit. To have a fixed illumination of the first surface the axis of the Bragg angle has to lie on the surface of the first crystal.
- Yaw and roll of the crystal ( $\phi$  and  $\chi$ ): They are only needed to correctly position the crystal with respect to the beam to limit the misalignment effects.
- Transversal translation of the crystal ( $X$ ) The crystal blocks must be shifted in the transversal ( $X$ ) direction to select the channel-cut crystal which will be used in a given experiment.

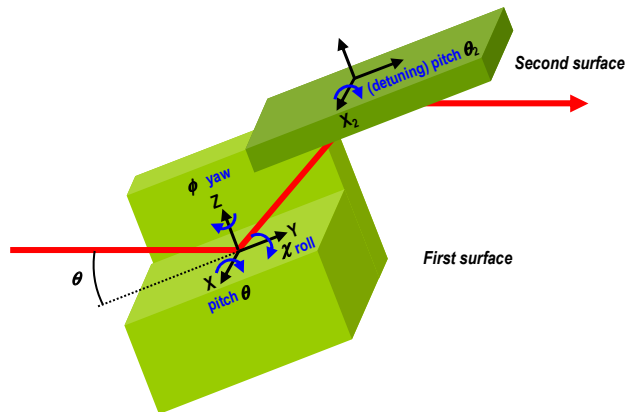


**Figure 20.** Definitions of orientations and rotations of the monochromator. Definitions are also valid for the KB mirrors.

### 5.2.4 Misalignments in a channel-cut design

Misalignments on the position of the crystal block lead to deviations of the beam position and energy shifts. The monochromator has to be aligned in such a way that:

- The beam shall not shift significantly in the transversal direction in energy scans. This shift is due to roll misalignments.
- The effective value of the Bragg angle on the crystals does not differ significantly from the nominal one. This is ensured by limiting the yaw and roll misalignments of the crystal.
- The rotation axis that sets the Bragg angle lies on the surface of the first crystal surface, or at any determined location. This is important to be able to predict the height of the beam at the exit of the monochromator from the value of the set-up energy (and thus from the Bragg angle) using expressions in section 5.2.1.

These three conditions to correctly orientate position the channel cut crystal are quantified below.

#### 5.2.4.1 Lateral shift of the beamline in energy scans

The beam shifts transversally due to roll misalignments. In the case of the channel-cut monochromator, as the two crystal surfaces are parallel, they have the same roll angle. In this case, if the roll axis is collinear with the beam axis (which is true if the beam is not deflected before the monochromator, as it is the case in XALOC), the beam is only shifted transversally during the path between the crystal surfaces. Moreover, since a constant transversal shift is not an issue for alignment purposes, one has to optimise only the difference of the transversal shift of the beam when scanning the energy, that is,

$$\Delta x = 2 \chi \Delta h$$

where  $\chi$  is the roll misalignment of the channel cut crystal and  $\Delta h$  is the difference in the beam height in the whole energy range, which is less than 2 mm (Fig. 23). Therefore, a roll misalignment of  $\chi = 0.25$  mrad will produce a lateral beam shift of about 1  $\mu\text{m}$ , significantly smaller than the horizontal beam size.

#### 5.2.4.2 Misalignments affecting Bragg angle value: yaw and roll

Due to orientation errors of the monochromator crystals (pitch, yaw and roll), the effective Bragg angle of the crystals with respect to the incoming beam will be different than the nominal value. A conservative estimate of the effective Bragg angle of the first crystal taking into account the orientation errors and the beam divergence is [4]

$$\theta_1 - (\theta_0 - \Sigma'_y) = \frac{1}{2} (\Sigma'_x{}^2 + \chi^2) \tan \theta_0 + \frac{\chi}{\cos \theta_0} \Sigma'_x + \phi \chi,$$

where

$\theta_0$       Rotation (Bragg) angle

$\Sigma'_x$       Beam horizontal divergence

$\Sigma'_y$	Beam vertical divergence
$\chi$	Roll of the crystal block
$\phi$	Yaw of the crystal block

To put some numbers, if  $\theta_0 = 30^\circ$ ,  $\Sigma'_x = 0,22$  mrad (i.e., twice the horizontal FWHM beam divergence), and  $\chi$  and  $\phi$  are aligned to an accuracy better than  $\pm 1$  mrad, the deviation of Bragg angle of the first crystal due to misalignments will be less than  $2 \mu\text{rad}$ , which is well below to the Darwin width of the Si(111) crystals.

#### 5.2.4.3 Height of the Bragg angle axis respect to the first crystal surface

Previous expressions assumed that the rotation axis that sets the Bragg angle was lying on the surface of the first crystal. Strictly speaking, this is not necessary to correctly align the monochromator, as other analytical expressions could be found in the case that the Bragg angle axis had an offset. However, regardless the location of the Bragg angle axis, the offset has to be known to be able to predict the beam height dependence on the energy. Any uncertainty leads to a misalignment of the beam height at the exit of the monochromator.

Let's evaluate the effect of this misalignment. Assume that the axis setting the Bragg angle has a known position within an uncertainty of  $\Delta A$  along the crystal surface normal direction. The resulting uncertainty in the beam height is then

$$\Delta h_A = 2 \Delta A \cos \theta.$$

Assuming we align the crystal surface with respect to the axis setting the Bragg angle to a uncertainty of  $\Delta A = \pm 2 \mu\text{m}$ , the uncertainty of the beam height will be  $\Delta h_A < \pm 4 \mu\text{m}$ . The vertical demagnification done by the vertical focusing mirror ( $M_v \sim 4$ ) reduces the uncertainty of the vertical position of the beam to  $\pm 1 \mu\text{m}$  at sample position, which is acceptable.

### 5.3 Power load

The first crystal of the monochromator will absorb all the power transmitted through the previous elements (Front-end, white beam slits, vacuum window and diamond filter). See table 5 for the summary of the power loads on the crystal under the worst-case (white beam slits fully open, the storage ring operating at 400mA) and working conditions (slits closed to mirror acceptance, which is  $112 \times 54 \mu\text{rad}^2$ , and a current of 250 mA in the storage ring).

In working conditions the calculated absorbed power is less than 50 W, whereas power densities range from  $3.7 \text{ W/mm}^2$  at 15 keV to  $7 \text{ W/mm}^2$  at 5 keV. These heat loads are well handled by Si(111) crystals with indirect cryogenic cooling. As an example, in a test at SPring8 the rocking curve width of a crystal absorbing 400W with a peak power density up to  $76 \text{ W/mm}^2$  was kept constant within only 1 arcsec ( $5 \mu\text{rad}$ ) [6]. In the same tests, when the heat load increased to 700 W, the rocking curve broadened by 4 arcsec ( $20 \mu\text{rad}$ ). Therefore, as this experiment and other results at the ESRF combining measurements and calculations have shown [7], the power and power densities yielded in the monochromator under working conditions can be efficiently evacuated by the state-of-the-art cryocooling systems without introducing a significant thermal bump in the crystal surface

In the worst-case conditions, maximum power densities are the same as in the working conditions, and only total absorbed power increases to about 600 W without the diamond window. The total amount of power absorbed represents a tougher requirement, but is still manageable by an indirect cryogenic cooling as mentioned experiments have already proven.

Regarding the power footprint, it changes with energy in the longitudinal (Y) direction. At 5 keV the footprint is about  $10.5 \times 10 \text{ mm}^2$ , while at 15 keV it increases to  $10.5 \times 32 \text{ mm}^2$ , when white beam slits are fully open.

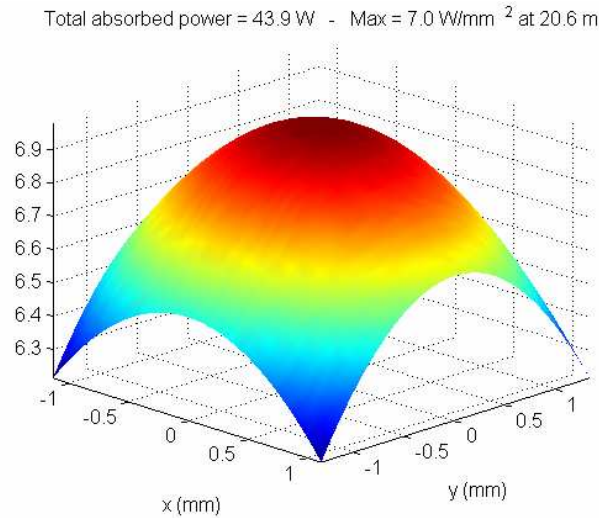


**Figure 21.** Spatial power distribution absorbed by the first crystal of the monochromator at 5 keV (Bragg angle  $23.296^\circ$ ) in working conditions (i.e. current of 250 mA in the storage ring and slit acceptance reduced to 1 FWHM of the beam divergence horizontally and 2 FWHM vertically). The beam is attenuated by a  $300\mu\text{m}$ -thick diamond vacuum window.

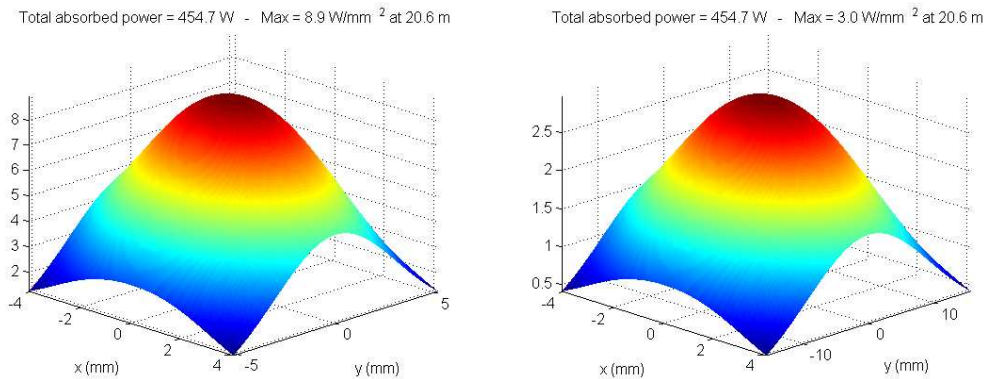


**Figure 22.** Spatial power distribution absorbed by the first crystal of the monochromator when the selected energy is 5 keV (*left*) and 15 keV (*right*) in the worst-case conditions. Bragg angles are  $23.3^\circ$  and  $7.57^\circ$ , respectively. The beam is previously cut by the front end, and attenuated by the  $300\mu\text{m}$ -thick diamond vacuum window and the  $300\mu\text{m}$ -thick diamond crystal in Laue geometry (effective thickness is  $311.8 \mu\text{m}$ ).

## 6 The focusing optics: KB mirror mounting

### 6.1 Functionality

The monochromatized beam is focused onto the experimental set-up (either the sample, the detector, or at some point along the optical axis nearby) by two mirrors in a Kirkpatrick-Baez configuration [5]. In this configuration each mirror focuses meridionally in one dimension, so their nominal shape is an elliptical cylinder. The thermal load on the mirrors is negligible.

The vertical focusing mirror (VFM) and the horizontal focusing mirror (HFM) will be placed at 23.3 m and at 25.5 m, respectively, from the source. Both are coated with Rh have a nominal grazing incidence angle of the beam with respect to the surface of  $0.235^\circ$  (4.1 mrad). The reflectivity of the mirrors is around 0.9 in the whole energy range, with a cut-off energy of about 16 keV (Fig. 23).

The mirrors focus the source nominally at a distance  $q_v = 6.075$  m and  $q_h = 3.875$  m, for the VFM and the HFM, respectively. The demagnification of the source is then  $M_v = 3.84$  and  $M_h = 6.58$  in the vertical and the horizontal plane, respectively. Nevertheless, the focus has to change in a limited range to be able to focus either on the sample or the detector, which can be at different distances from the sample (typically in the range of 0.07-0.7 m).

The useful optical length of the VFM and HFM mirrors is 300 mm and 600 mm, respectively. The VFM accepts the entire beam, whereas the HFM accepts 1 horizontal FWHM of the beam. This length of the HFM appears to be a good compromise between acceptance and handiness, optical properties and cost.

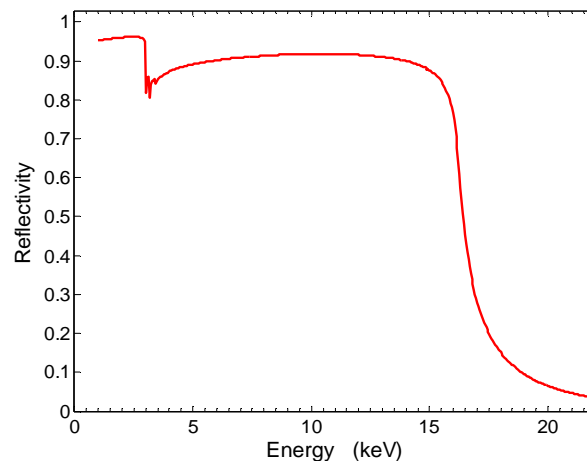


**Figure 23.** Reflectivity of the KB mirrors. The mirrors are coated with Rh and have a grazing incidence angle of  $0.235$  deg (4.1 mrad).

### 6.2 Beam footprint

The VFM has a footprint of 143 mm FWHM longitudinally and 2.7 mm transversally (Fig. 24 *left*). The footprint of the HFM is much longer than the VFM, due to the larger divergence of the source in this dimension. This implies in practice that the beam is cut by the horizontal acceptance of the HFM, which is 600mm. This represents approximately the FWHM of the beam (Fig. 24, *right*).

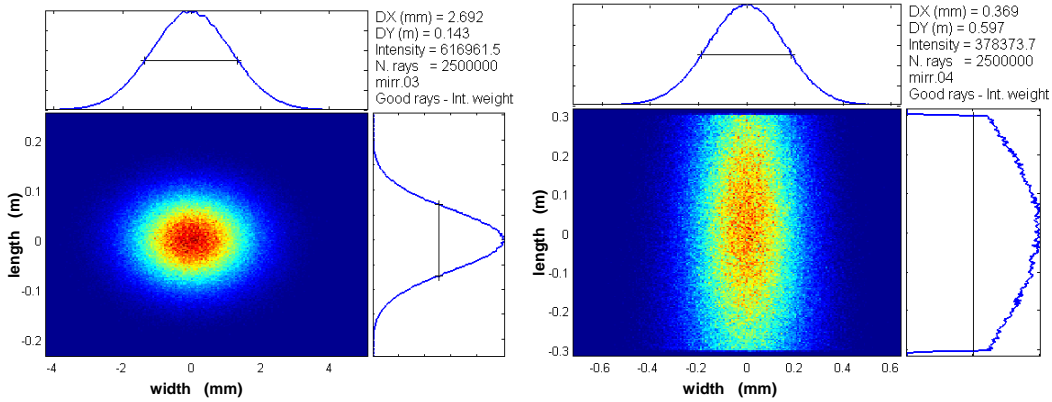


**Figure 24.** Beam footprint on the vertical (*left*) and horizontal (*right*) focusing mirrors. The beam is cut in the horizontal dimension by the acceptance of the HFM.

### 6.3 Effect of the slope errors

#### 6.3.1 Short-period slope errors

The effect of slope errors having short periods compared with the footprint of the beam on the mirror is a broadening of the focused beam. At focus the induced broadening is

$$\sigma_{z, slope} = 2 q_z \sigma'_{slope}$$

where  $q_z$  is the distance between the optical element and the focus in the  $z$  direction, and  $\sigma'_{slope}$  is the RMS slope errors in this direction. This contribution is to be added quadratically to the focal size resulting from the demagnification of the source. As typically the focusing distance is about 5 m, by limiting the RMS slope error up to a few  $\mu\text{rad}$ , when working under these conditions the beam is not severely broadened by slope errors. Moreover, the beam preserves the gaussian profile.

When working out of focus, beam inhomogeneities arise. However, these are only important when working very far from focal condition and in the vertical dimension, in which the blurring effect induced by the emittance of the source is smaller.

#### 6.3.2 Long-period slope errors

Long-period slope errors, i.e. those with periods longer than about 1/10 of the footprint of the beam on the mirror, do not simply expand the beam as short-period errors do, but rather change the beam profile losing the original gaussian shape. These beam inhomogeneities are especially important when the beam is defocused, as is it planned in the XALOC beamline to match the beam size to the crystal dimension, and in the vertical plane due to small source size and divergence.

As an example, let's model the beamline introducing different slope errors with realistic profiles and RMS values (Fig. 25). Raytracing calculations give completely different values of the beam sizes at sample and in focus depending on the profile of the slope errors at low frequencies, even though RMS values are below 1  $\mu\text{rad}$ .

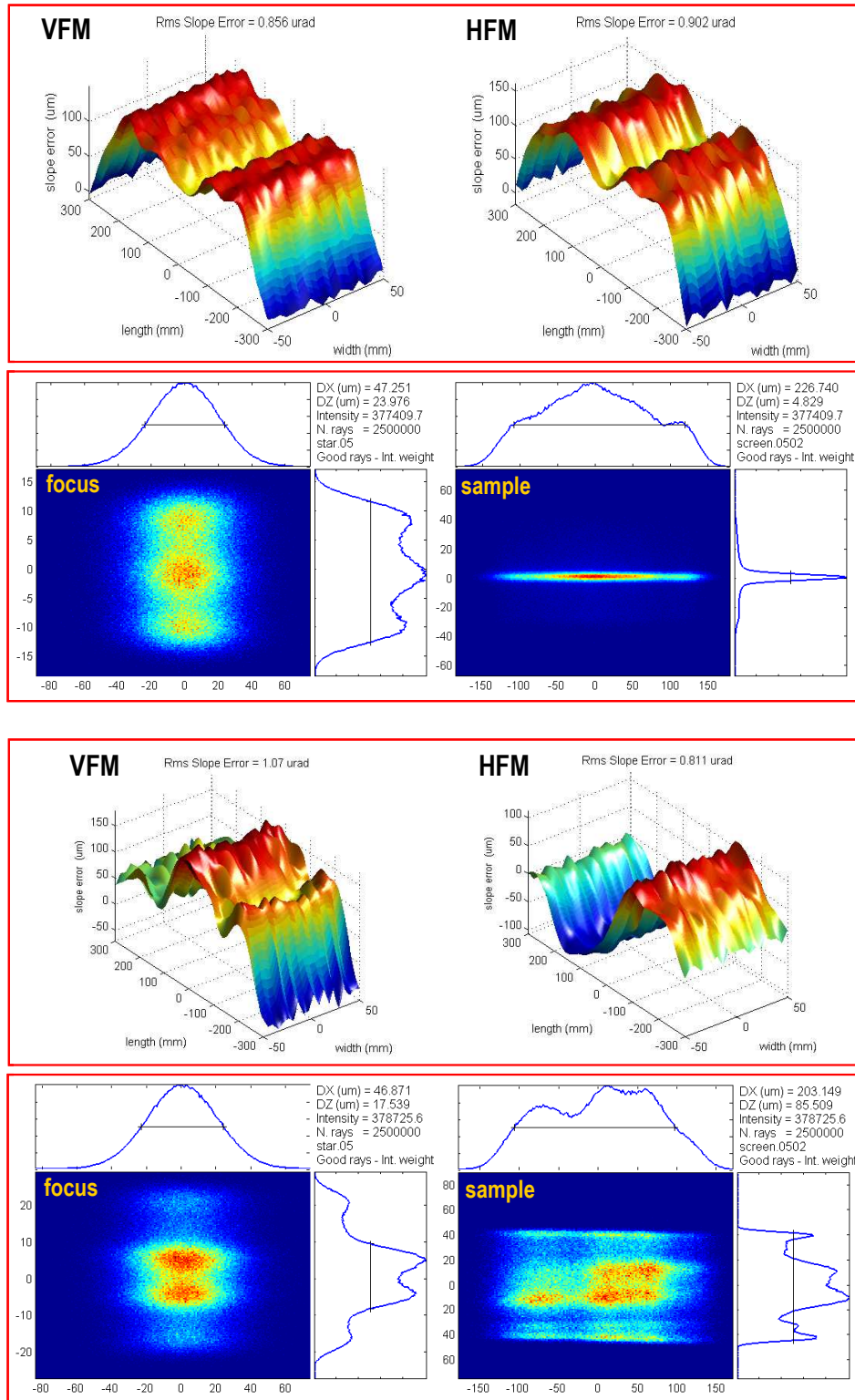


**Figure 25.** Two examples of the effect of long-period slope errors of mirrors (*above*) Modelled slope error profiles for the VFM and HFM. (*below*) Resulting modelled beam spots at focal (*left*) and at sample (*right*) positions. The values are to be compared with the model of the beamline without slope errors (Fig. 7).

Example raytracing calculations show (Fig. 26) that the beam homogeneity is specially affected by slope errors with periods longer than 20 mm in the vertical plane and longer than 150 mm in the horizontal one. These periodicities correspond roughly to 1/7 and 1/4 of the FWHM of the footprint on the VFM and HFM, which are 143 mm and 600 mm, respectively.

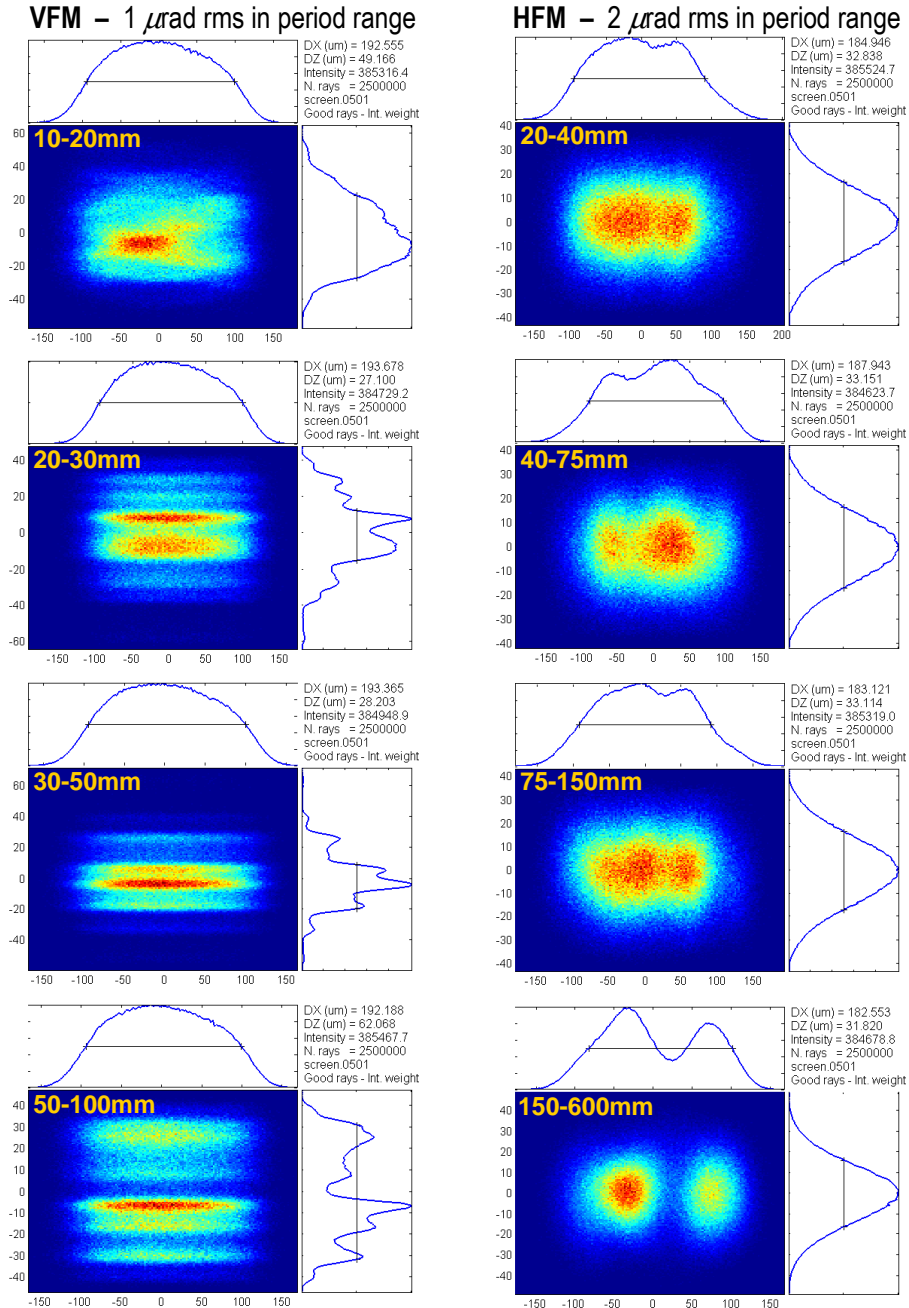


**Figure 26.** Example of raytraced beam spots at sample position (379 mm before focus) showing the influence of the periodicity of the slope errors. (*Left column*) An RMS slope error of 1  $\mu$ rad is assumed in the VFM in the specified period range (from up to bottom, 10-20 mm, 20-30 mm, 30-50 mm and 50-100 mm). The profile is highly inhomogeneous at periodicities above 20 mm. (*Right column*) Same for the HFM with a RMS slope error of 2  $\mu$ rad in the specified period range (from up to bottom, 20-40 mm, 40-75 mm, 75-150 mm and 150-600 mm). The profile becomes inhomogeneous at periodicities above 150 mm.

In conclusion, the control of long-period slope errors and the handling of the beam unhomogeneities caused by them is a critical issue for the beamline optics design. Careful consideration of the quality of the mirrors is mandatory. Ideally, specification of the mirrors should be made through the Power Spectral Density (PSD) or, at least, include the maximum allowed slope error generated by the long-period slope errors which affect the homogeneity of the beam spot.

### 6.3.3 Reducing the effect of long-period slope errors

#### 6.3.3.1 Removing the VFM

In case the vertical unhomogeneities affected the quality of data, the VFM could be removed from the beam path. In this case, as the beam remains unfocused in the vertical direction, vertical beam size at sample increases to  $710 \mu\text{m}$  FWHM (Fig. 9), but preserving the gaussian profile given by the source. Beam should be adjusted using slits close to the sample. An additional advantage of removing the VFM is that the vertical beam divergence is that of the source, which is as low as  $25 \mu\text{rad}$  FWHM.

#### 6.3.3.2 Reducing the grazing incidence angle

Reducing the grazing angle of incidence on the mirror spreads the footprint along the mirror. This is usually considered adverse as the mirror has to be longer to collect the same fraction of the beam. However, spreading the footprint along a longer surface averages the slope errors, so their effect on the spot at sample is to broaden the beam profile and smoothing the unhomogeneities.

This is illustrated in figure 27, in which the beam spots at 379 mm before focus are shown for 2 different coatings and incidence angles of the VFM, but with the same slope errors. The spot produced by a shallower angle of incidence onto the VFM is broader and more homogeneous.

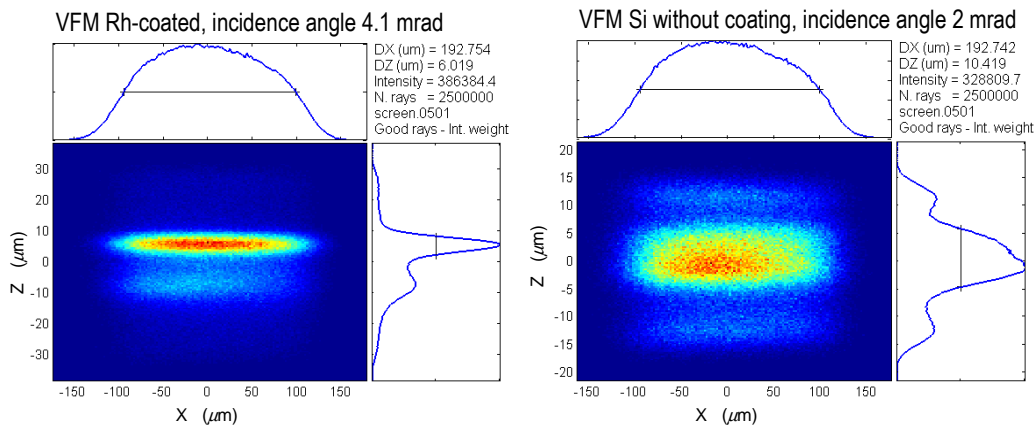


**Figure 27.** Example showing the influence of the footprint on the beam spot out of focal position (spot at 379 mm before focus). In both pictures RMS slope errors of the VFM are  $1 \mu\text{rad}$ . (left) VFM is coated with Rh, with an incidence angle of the beam onto the mirror of 4.1 mrad (right) VFM not coated (reflectivity given by substrate made of Si), with an incidence angle of the beam onto the mirror of 2.0 mrad. The modelled slope error profile is the same in both cases.

### 6.3.3.3 *Use of optics locally corrected*

The local correction of the optical surface allows reducing the amplitude of slope errors having relatively long periods. Several methods are in use to correct locally optical surfaces. Currently available ones are

- Iterative polishing: the surface is iteratively polished and measured to find local defects. After several iterations, slope errors with long periods are reduced
- Use of adaptative optics. Adaptative (bimorph) mirrors have the capability to modify the surface through piezoelectric actuators so that long-period slope errors are reduced. Only periods above twice the length of the actuator (currently ca.  $2 \times 20 = 40$  mm) can be corrected.

The strategy chosen in XALOC to reduce the effect of slope errors, and in particular those having long periods, depends on the capabilities of the companies tendering for the KB mirrors.

## 7 **Summary**

- The beamline has to be able to cope with relatively large crystals, while keeping high resolution in reciprocal space (needed for large unit cells), and at the same time to satisfy the needs of the user community which usually requires small crystals. To this aim an optical design comprising a flexible focal spot that may be adapted to the sample geometry has been designed.
- The beam size should be adjusted to match the dimensions of the crystals to be measured. Consequently the beam dimensions at sample position are adjustable in the range 20-200  $\mu\text{m}$ . Larger dimensions within this range will be reached by defocusing.
- The beamline will be tuneable (5-15 keV) and optimized at the Se K-edge (12.658 keV) to exploit anomalous diffraction.
- The source will be a PPM in-vacuum undulator with a period of 21.3 mm and a minimum gap of 5.5 mm. The calculated flux on sample is about  $5 \cdot 10^{12}$  ph/s.
- The Front-end has an acceptance of  $0.4 \times 0.2 \text{ mrad}^2$  (H $\times$ V), which transmits to the beamline a total power of 1.49 kW at current of 400 mA in the storage ring.
- The first active optical element of the beamline is a 300 $\mu\text{m}$ -thick diamond vacuum window. This removes about half of the incoming power.
- The beamline optics consists in a diamond crystal filter, a channel-cut monochromator and a KB focusing optics.

### *Ancillary branch*

- As an option, an ancillary branch for testing and instrumentation development is considered in the case resources allow it.
- A 300 $\mu\text{m}$ -thick diamond filter will reduce the amount of power received by the channel-cut monochromator. In addition, this filter will act as a Laue monochromator, which will provide the monochromatic beam that feeds the ancillary branch.

- The beam of the ancillary branch will have a fixed wavelength (1.37 Å, 9.041 keV). The Laue monochromator will be tilted 15.815° with respect to the incoming beam. The monochromatic beam will be diffracted at an angle of  $2\theta = 38.9^\circ$  using the (111) reflection.
- No further optics is foreseen at this moment for the ancillary branch. Therefore, the monochromatic beam of this branch would come to an experimental hutch with a low divergence ( $0.1 \times 0.03 \text{ mrad}^2 \text{ H} \times \text{V}$ ) and relatively large spot size ( $0.8 \times 0.6 \text{ mm}^2 \text{ H} \times \text{V}$ ).

#### *Monochromator*

- The photon energy of the beamline is selected by a symmetric Si(111) channel-cut monochromator in a non-dispersive arrangement.
- The total power absorbed by the monochromator when slits are closed to match the acceptance of the mirrors is 71.5 W at 400 mA in the storage ring. The maximum power density is  $11.8 \text{ W/mm}^2$ . If slits were fully open to accept all the power coming from the Front-End, the monochromator would absorb 687 W. In any case, cryocooling is required.
- Beam size (FWHM) at focal position is  $44 \times 4 \text{ } \mu\text{m}^2$ . At sample position (considered to be 379 mm before the focus) the beam sizes are  $225 \times 37 \text{ } \mu\text{m}^2$ .

#### *Kirkpatrick-Baez (KB) Mirrors*

- A KB configuration is used to focus the beam on the sample or the detector. The mirrors are Rh-coated and have an incidence angle of 4.1 mrad with respect to the beam.
- The meridional dimensions of the active optical surfaces of both mirrors (horizontal focusing mirror, HFM, and vertical focusing mirror, VFM) are respectively 600 and 300 mm. The HFM can collect about 1 FWHM of the beam in the horizontal dimension, whereas in the vertical dimension the VFM collects all the beam.
- The VFM shall be removable from the beam path. When this mirror is removed, the beam arrives vertically unfocused to the sample, with a large vertical size (710 mm FWHM) and a low vertical divergence (about  $25 \text{ } \mu\text{rad}$ ).
- Long-period slope errors affect the homogeneity of the beam, losing the gaussian profile given by the source. The effect is especially critical when working out of focus and in the vertical plane.
- VFM could be uncoated and having a shallower angle of incidence of the beam (around 2 mrad) if beam inhomogeneities due to slope errors were shown to be less important.
- Control of the long-period slope errors and handling of the beam inhomogeneities caused by them are critical issues for the beamline optics design. Careful consideration of the quality of the mirrors and of the possible adaptive optics solutions is mandatory.

## 8 Bibliography

- [1] Bertwistle D, *Conceptual Design of a 21.3mm-Period In-Vacuum Pure Permanent Magnet Undulator*, ALBA internal report.
- [2] Nicolás J, *Energy spread effects on source divergence for undulators*, ALBA internal report.
- [3] Lai B and Cerrina F, *Nucl. Instrum and Methods* **A246**:337-341 (1986).
- [4] *CLS 06-ID-1 XAFS Beamline Preliminary Design Report*. Internal report CLS- Design Note – 6.2.78.2 Rev. 0
- [5] Kirkpatrick P and Baez AV (1948), *J. Opt. Soc. Am.* **38**:766-774.
- [6] Sanchez del Río M, Gruebel G, Als-Nielsen J and Nielsen M, *Rev. Sci. Instrum.* **66**(11):5148-5152 (1995).
- [7] Mochizuki T, Kohmura Y, Awaji A, Suzuki Y, Baron A, Tamasaku K, Yabashi M, Yamazaki H and Ishikawa T, *Nucl Instr. and Meth.* **A467**:647-649 (2001).
- [8] Zhang L, Lee W-K, Wulff M and Eybert L, *J. Synchrotron Rad.*, **10**:313-319 (2003).